



TITLE:

Full-particle simulations of instabilities in a thin current sheet of the magnetospheric system prior to substorm onset Space science

AUTHOR(S):

Uchino, Hirotoishi; Machida, Shinobu

CITATION:

Uchino, Hirotoishi ...[et al]. Full-particle simulations of instabilities in a thin current sheet of the magnetospheric system prior to substorm onset Space science. Earth, Planets and Space 2015, 67: 165.

ISSUE DATE:

2015-10-08

URL:

<http://hdl.handle.net/2433/210414>

RIGHT:

© 2015 Uchino and Machida. This article is distributed under the terms of the Creative Commons Attribution 4.0 International License (<http://creativecommons.org/licenses/by/4.0/>), which permits unrestricted use, distribution, and reproduction in any medium, provided you give appropriate credit to the original author(s) and the source, provide a link to the Creative Commons license, and indicate if changes were made.

FULL PAPER

Open Access



Full-particle simulations of instabilities in a thin current sheet of the magnetospheric system prior to substorm onset

Hirotochi Uchino^{1*} and Shinobu Machida²

Abstract

Substorm triggering was the focus of recent two-dimensional superposed-epoch analyses based on Geotail and THEMIS data. The results indicate that magnetic-field dipolarization at $X \sim -8$ Re and magnetic reconnection at $X \sim -20$ Re occur simultaneously at the onset. These results imply that there are physical mechanisms that widely affect both the dipole and current-sheet regions. The analyses also have found that a local B_z enhancement appears before the substorm onset and magnetic reconnection occurs at its tailward edge. We performed four 2.5-dimensional full-particle simulations with a new initial magnetic-field structure to focus on instabilities in the magnetosphere. The structure is similar to the Earth's dipole magnetic field combined with a stretched field and current sheet on the tailward side. The simulation with the initial magnetic-field configuration shows that nodes of the magnetic field appear in the current sheet where the growth condition of tearing instability is satisfied. The features of the instability are close to those of the electron tearing mode reported in previous simulation results. Another three simulations with a local B_z enhancement, as seen in the observational results, at various locations in the current sheet were performed to explore its impacts on the evolution of the instability. A relaxation process around the enhancement generates a new node at its tailward edge if its location satisfies the growth condition. The wavelength and dominant mode of the instability can be changed by the coupling between the process and tearing mode depending on the location of the enhancement. Our simulations reveal new features associated with tearing instabilities in the magnetospheric-field configuration.

Keywords: Tearing instability; Magnetospheric substorm; Magnetic reconnection

Background

Magnetospheric substorms are manifestations of a general physical process that causes drastic changes in both the magnetosphere and ionosphere. Akasu (1964) first illustrated the time development of the auroral substorm by using data collected during the International Geophysical Year. Although a number of substorm-triggering models have been proposed on the basis of observational evidence (Lui 1991), none can as yet perfectly explain the mechanism responsible for substorm triggering.

One of the triggering models is the “near-Earth neutral line” (NENL) model (Baker et al. 1996; Hones 1979),

which has been used successfully to explain energy transfer during substorms from the magnetic field to particles in the magnetotail. The cross-tail current becomes thinner as the convective electric field penetrates into the magnetosphere through the southward turning of the interplanetary magnetic field, and magnetic reconnection occurs at the NENL. The earthward flow generated by the magnetic reconnection injects energetic particles into the inner magnetosphere and causes dipolarization (Shiokawa et al. 1998). Another triggering model is the “current disruption” (CD) model (Chao et al. 1977; Lui 1996), which adopts CD as the cause of the field-aligned current flowing into the Earth's ionosphere. The process is initiated by a cross-field current instability at $X \sim -8$ Earth radii (Re; 1 Re = 6378 km). A rarefaction wave ejected from the CD region propagates tailward and induces

*Correspondence: uchino@kugi.kyoto-u.ac.jp

¹Department of Geophysics, Kyoto University, Kyoto, Japan

Full list of author information is available at the end of the article

current-sheet (CS) thinning. A magnetic reconnection arises at $X \sim -20$ Re as the consequence of the process.

Machida et al. (2009, 2014) performed superposed-epoch analyses with Geotail and THEMIS data to investigate the physical conditions in the magnetotail around the substorm onset. They have suggested a new substorm-triggering model, namely, the “Catapult Current Sheet Relaxation” (CCSR) model, based on the results. This model has the following characteristics: (1) magnetic-field dipolarization and magnetic reconnection occur simultaneously (within 1–2 min) with auroral breakup; (2) from 4 min before substorm onset, the CS relaxes around $X \sim -13$ Re; and (3) a local B_z enhancement coincides with the CS relaxation at $X \sim -17$ Re and magnetic reconnection occurs on the tailward edge of the enhancement. These results are indicative of the need for physical mechanisms that cover a wide area and span the range from the dipole-like (DL) region to the CS region.

A number of particle simulations have been performed to study the physical processes associated with magnetic reconnection in order to investigate the causes of substorm triggering (Birn et al. 2001; Hesse et al. 1999; Kuznetsova et al. 2001). Particle simulations, where the initial magnetotail-like structure is described by a slightly modified Harris with a normal magnetic field to the CS, have led to the conclusion that tearing modes may lead to magnetic reconnection under specific physical conditions (Dreher et al. 1996; Zwingmann et al. 1990). Pellat et al. (1991) indicated that electrons magnetized by the normal magnetic field to the CS suppress the tearing mode with realistic physical values. Recent simulation studies that impose the convective electric field as a boundary condition at the magnetospheric lobe have shown that tearing instability and magnetic reconnection can be driven (Liu et al. 2014; Pritchett 2005). Sitnov and Swisdak (2011) showed that the “X-point” (the point where oppositely directed magnetic-field lines reconnect) of magnetic reconnection forms on the tailward side of the B_z -hump in the CS, as was found by Machida et al. (2009; 2014), because the electric energy of the Poynting flux is locally concentrated. The observational results reported in Machida et al. (2009; 2014), however, require simulations of both the DL field and the CS region.

Therefore, we performed four 2.5-dimensional full-particle simulations with a new initial magnetic-field structure in order to focus on instabilities in the magnetosphere. The structure is similar to the Earth’s dipole magnetic field combined with a stretched magnetic field and CS on the tailward side. The first simulation does not have a local B_z enhancement, as seen in the observational results (Machida et al. 2009, 2014), in its initial condition. We discuss the process leading to the appearance of instabilities, as well as the growth rate and wavelength

of the modes resulting from such inhomogeneous initial magnetospheric-field conditions. We also conducted three other simulations with a local B_z enhancement at various locations in the CS. Based on the simulation results, we discuss the effects of the presence of the B_z enhancement on the resulting instabilities.

Simulation settings

The 2.5-dimensional full-particle simulations were performed in the presence of a characteristic magnetic-field structure corresponding to a DL field region that is connected to the magnetotail region. We have set periodic boundary conditions in both the x (Sun–Earth) and z (north–south) directions of the geocentric solar magnetospheric coordinate system. Our “2.5-dimensional” setup means that two dimensions cover real space, while the particle-velocity and electric/magnetic-field vectors have three dimensions. To quantify the particle motions, the Lorentz equation is solved by using the Buneman–Boris method. Maxwell’s equations are solved based on the fast Fourier transform (FFT) method (Birdsall and Langdon 1985). In this paper, we refer to the positive (negative) x direction as “earthward” (“tailward”), in accordance with the terrestrial magnetotail picture.

Figure 1a shows the magnetic-field structure, which is defined by the following vector potentials:

$$A_y(x, z) = A_{y0}(x, z) + A_{y1}(x, z), \quad (1)$$

$$A_{y0}(x, z) = B_0 d \ln \left[\frac{\cosh\left(\frac{z}{d}\right) + p \cos\left\{2\pi\left(-\frac{x}{2\pi d} + \frac{1}{2}\right)\right\}}{\sqrt{1-p^2}} \right] \quad (-\pi < x/d < 0), \quad (2)$$

$$A_{y0}(x, z) = B_0 d \ln \left[\frac{\cosh\left(\frac{z}{d}\right) + p}{\sqrt{1-p^2}} \right] \quad (-4\pi < x/d < -\pi), \quad (3)$$

$$A_{y1}(x, z) = -\epsilon_1 B_0 D \exp\left(-\frac{z^2}{d^2}\right) \quad (-\alpha/d < x/d < 0), \quad (4)$$

$$A_{y1}(x, z) = -\epsilon_1 B_0 \left\{ -C \left(\frac{x+\alpha}{d} \right) + D \right\} \exp \left\{ E \left(\frac{x+\alpha}{d} \right) - \frac{z^2}{d^2} \right\} \quad (-4\pi < x/d < -\alpha/d), \quad (5)$$

where d is the CS half-thickness. We use $p = 0.4$ ($0 \leq p < 1$, this value controls the roundness of the DL magnetic field; when $p = 0$, the magnetic-field structure is the Harris solution, for example), so that the maximum

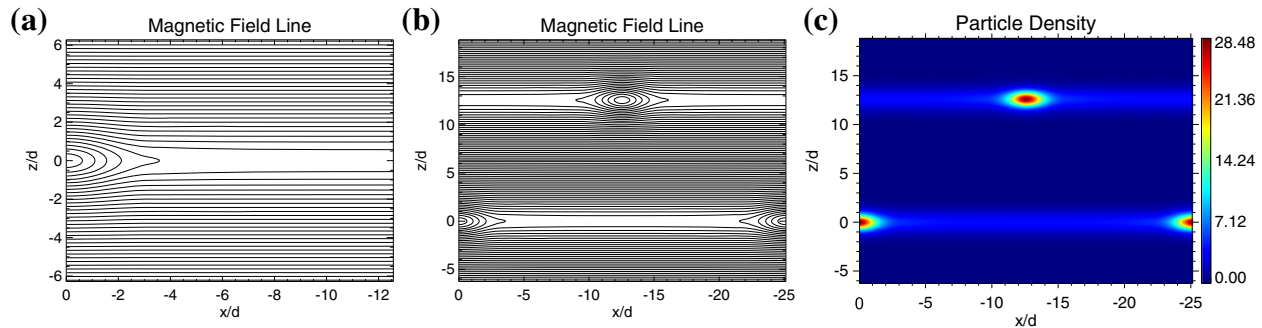


Fig. 1 Initial configurations of the simulations. **a** Initial condition of the magnetic-field line selected in the *lower left* of the simulation system and **b** in the overall system of Run(0). **c** Hot-particle distribution (n_h) determined by the numerical “quiet start” method

B_z field in the DL region is about a half of the magnetic field in the lobe region ($B_0 = 1$). Other parameters are $\epsilon_1 = 0.03$ (the ratio of A_{y1} to A_{y0}), $C = 10d/3$, $E = 3/4$, $D = C/E = 40d/9$, and $\alpha/d = \pi - 1/E \sim 1.8$. The main field given by A_{y0} corresponds to Earth’s DL magnetic field ($-\pi < x/d < 0$) and the magnetic field of the CS in the magnetotail ($-4\pi < x/d < -\pi$). The field defined by A_{y1} corresponds to the finite northward-directed component of the magnetic field in the CS; its effects are described in this section.

The DL field of A_{y0} is represented by a modification of the “Kelvin’s cats eyes (KCE)” magnetic field (Schindler 2007), which satisfies the magnetohydrostatic (MHS) conditions in two-dimensional (2D) space. This KCE field is obtained by setting $f(\zeta) = \{\exp(i\zeta) + p\}/\sqrt{1-p^2}$ ($\zeta = x + iz$) in the analytical solution of the Grad–Shafranov equation, i.e.,

$$A_y(x, z) = \ln \frac{1 + |f(\zeta)|^2}{2 \left| \frac{df}{d\zeta} \right|}, \quad (6)$$

under the condition that particles follow a Maxwell velocity distribution. The KCE field has the following functional form:

$$A_y(x, z) = \ln \left(\frac{\cosh(z) + p \cos(x)}{\sqrt{1-p^2}} \right). \quad (7)$$

There are two advantages in regard to the use of the KCE field. First, because the B_z component derived from Eq. (2) always becomes 0 at $x/d = -\pi$ along z , we can easily define the magnetic configuration of the CS, which is connected to the DL field, by keeping the values of the B_x and B_z components constant on the tailward side of $x/d = -\pi$. Equation (3) expresses the constant B_x and B_z in the x direction. Second, periodic boundary conditions can be applied to the KCE field because $B_z = 0$ and $\partial B_z / \partial x = 0$ at $x = 0$. The magnetic configuration of the initial conditions in the overall simulation system is shown in Fig. 1b. This configuration is obtained by

reversing the magnetic field shown in Fig. 1a (which displays the lower left quadrant of the simulation system) and applying this to the entire region. Figures of simulation results for the simulation system display only the same region as Fig. 1a because the residual region had almost symmetrical structures owing to the periodic boundary conditions.

The physical parameters are defined as follows. The ion-electron mass and temperature ratio are $m_i/m_e = 100$ and $T_i/T_e = 4$, respectively. The ratio of the electron gyro-frequency to the electron plasma-frequency is $\Omega_e/\omega_{pe} = eB_0/(m_e\omega_{pe}) = 1$. We adopt $d = 0.5\delta_i = 5c/\omega_{pe}$ (δ_i : average ion inertial length in the simulation system) as the CS half-thickness. The spatial scales of the simulation system are normalized by d . This simulation box has a size of $L_x/d \times L_z/d = 8\pi \times 8\pi$ and covers 1024×1024 grid points, but the region shown in our figures is restricted to half of those ranges in both the x and z directions ($L_x/d \times L_z/d = 4\pi \times 4\pi$). The grid lengths Δx and Δz are constrained to $\Delta x = \Delta z = 0.1227c/\omega_{pe}$. The average number of particles in each cell is 25, where we adopt a ratio of the total number of hot to cold particles of 3:2. The cold particles are distributed homogeneously across the overall simulation system. We have used the relation $n_h(x, z) \propto \exp\{-2A_y(x, z)\}$ (Toichi 1972) to determine the positions of the hot particles carrying the diamagnetic current, which leads to the characteristic magnetic-field configuration. To assign positions of particles, we applied the “quiet start method” (Birdsall and Langdon 1985) to the relation and solved it by inversion. The cumulative distribution function $D(x, z)$ of the density function $n(x, z)$ is divided equally with respect to the total particle number N_p , and each particle position (x_i, z_i) (i : particle number, $1 \leq i \leq N_p$) can be obtained by solving the inverse of the relation $D(x_i, z_i) = i/N_p$. This procedure was performed numerically because it could not be done analytically because of the 2D setup. Figure 1c shows the hot-particle density across the entire simulation system resulting from the procedure. In regard to the a velocity distribution

for hot particles, we used the shifted Maxwellian, so the distribution function is

$$f_s = \frac{n(x, z)}{\pi^{3/2} v_{\text{th}s}^3} \exp \left[-\frac{v_x^2 + (v_y - U_s)^2 + v_z^2}{v_{\text{th}s}^2} \right], \quad (8)$$

where U_s is the drift velocity and $v_{\text{th}s}$ is the thermal velocity. U_s is calculated by using Ampere's law, $en(U_i - U_e) = \mu_0 \nabla \times B$, and the charge neutrality, $U_i/T_i = -U_e/T_e$. Furthermore, in order to quickly induce instabilities in the CS without unwanted electric-field effects in the specific simulation system, we have set smaller particle pressures than those of the magnetic field by a factor of 3, $v_{\text{th}s}^2 \equiv 2T_s/3m_s$. This setting is also effective to focus on couplings between the instabilities and relaxation process when a B_z local enhancement is included; this will be discussed further in "Discussion and conclusions" section.

Figure 2a shows the B_z component in the magnetic equatorial plane ($z/d = 0$). The B_z component of the DL magnetic field, B_{z0} , which is defined by A_{y0} , is shown as the purple line. B_{z1} , defined by A_{y1} , expresses the small positive normal B_z component that is present in the real magnetospheric CS. It is indicated by the green line. There is a discontinuity in the B_z differential at the boundary between the DL and CS regions ($x/d = -\pi$), which we henceforth refer to as the "DCB" (DL-CS boundary). This

discontinuity is formed by connecting the DL field and CS regions so that B_x is continuous at the location. The magnetic field in the CS region does not perfectly satisfy the MHS condition originally (i.e., it deviates from the Harris solution), so the transient adjustment of the CS initially appears in the E_y field. This discontinuity may be seen as unnatural, but it has been shown in a magnetohydrodynamical calculation that such a discontinuity can appear at the inner plasma-sheet boundary through penetration of the convective electric field during a substorm's growth phase (Voigt 1986). B_{z1} reaches its maximum value ~ 0.04 near the DCB and decreases toward the tail side. Electrons magnetized by normal magnetic field B_{z1} suppress the growth tearing mode (Pellat et al. 1991), so the region near the DCB is stable, while the stabilizing effect is less at the far tail. If we do not add B_{z1} to the simulation system, magnetic reconnection occurs at the location of the B_z differential discontinuity ($x/d = \pi$). The B_{z1} is useful to stabilize this reconnection, which is unimportant in the context of this study.

A time step of the simulation is $\omega_{pe} \Delta t = 0.2$, and we ran the simulation for 12,000 steps ($\Omega_i t = 24$). We call this simulation "Run(0)," since it serves as the reference simulation for the other runs in this study.

Observations of a magnetospheric CS during a substorm show that a region of local B_z enhancement appears

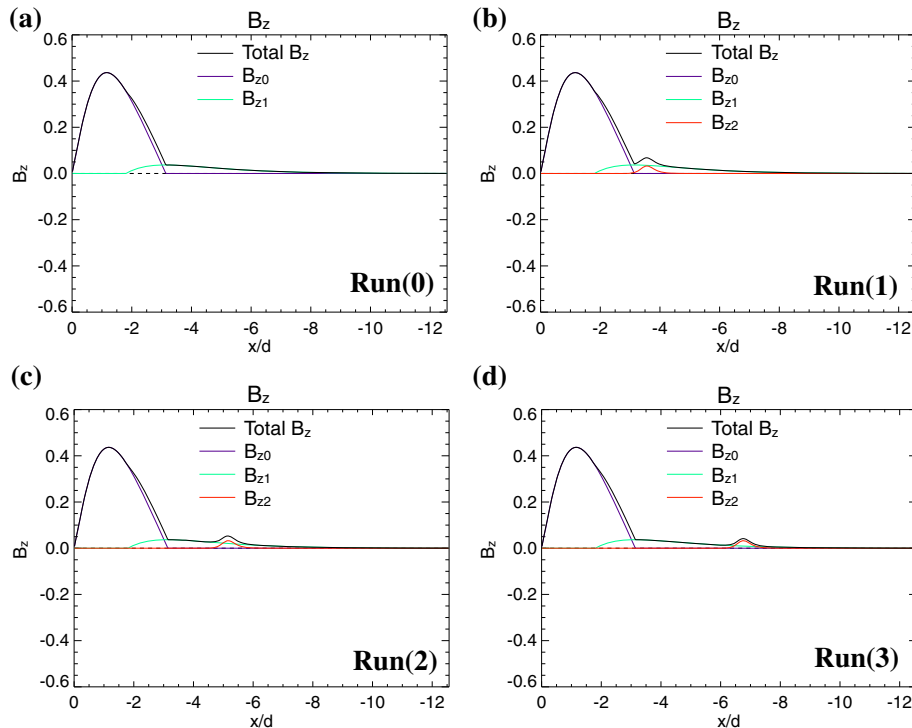


Fig. 2 Initial conditions of the B_z component in the equatorial plane ($z/d = 0$). **a–d** show the B_z component in Run(0)–(3), respectively. Purple lines indicate the magnetic field of the DL region B_{z0} , green lines indicate the small northward magnetic field in the CS B_{z1} , red lines express the enhancement of B_{z2} , and black lines show the total of B_z

at $X \sim -17$ Re a few minutes prior to substorm onset, and a magnetic reconnection occurs at the tailward edge of the enhanced region at the substorm onset (Machida et al. 2014). To investigate the effect of a local B_z enhancement in the CS, we have included such an enhancement in the CS of Run(0). We use the following vector potential, A_{y2} , to introduce the local B_z enhancement:

$$A_{y2}(x, z) = -\epsilon_2 B_0 \gamma d \exp\left(-\frac{z^2}{d^2}\right) \quad (-l_x < x/d < 0), \quad (9)$$

$$A_{y2}(x, z) = \epsilon_2 B_0 \gamma d \tanh\left(\eta \ln\left[-\frac{x + l_x}{\gamma d}\right]\right) \exp\left(-\frac{z^2}{d^2}\right) \quad (-4\pi < x/d < -l_x/d), \quad (10)$$

where $\epsilon_2 = 0.008$ (the ratio of A_{y2} to A_{y0}), $\eta = 4$ (this parameter controls the steepness of the local B_z enhancement), and $\gamma = 0.6$ (the width of the local B_z enhancement). Figure 2b–d shows the initial B_z configurations in the equatorial plane with the local B_z enhancement (B_{z2} ; red line), in addition to the initial conditions of Run(0). The maximum value of the local enhancement was set to approximately 10 % of the maximum of B_{z0} . We also set the width of the enhancement so as to constrain it to approximately one third of the width of the DL region, again based on observational results (Machida et al. 2014). The local maximum of B_{z2} appears at $x/d = -\gamma\{(2\eta - 1)/(2\eta + 1)\}^{1/2\eta - l_x}$. This value asymptotically approaches to $x/d \simeq -\gamma - l_x$ as η becomes greater than unity. We performed more than 10 simulation runs, but here we only show 3 relevant runs where the maximum location of the enhancement x_h/d has been shifted from $x_h/d \sim -3.6$ [Run(1)] to $x_h/d \sim -6.8$ [Run(3)] by changing the term l_x in intervals of $x/d \sim -1.6$ (see Table 1). The overall structures of the magnetic fields in the initial conditions in Run(1)–(3) are hardly distinguishable from that in Run(0). We also focus on the effect of a local B_z enhancement on instabilities, which depends on the locations where the enhancement is seeded in the CS.

Results

Instability in the current sheet

First, we mention that the stronger magnetic-field pressure causes CS thinning. Figure 3 shows the J_y profiles along z at $x/d = -8$ in Run(0) at times $\Omega_i t = 0.4$ and

$\Omega_i t = 4.0$ from the start of the simulation. J_y in the simulation, which is shown as the black line, initially follows the Harris solution with a half-thickness $d = 5c/\omega_{pe}$ (blue line). Because of compression due to the pressure difference, it proceeds to follow the thinner Harris profile for $d = 1.6c/\omega_{pe}$ (red line) as seen in Fig. 3b. The plasma pressure in the CS is 3 times smaller than that of the magnetic field, so the effective CS half-thickness has become $d' = 1.6c/\omega_{pe}$, which is about one third of the initial CS half-thickness. The CS in other runs becomes similarly thin.

Figure 4a, b displays the B_z component in the equatorial plane ($z/d = 0$), as well as the magnetic-field line and poloidal current, J_y , at times $\Omega_i t = 8.4$ and $\Omega_i t = 15.2$ in Run(0). The B_z value shown in Fig. 4a is averaged along the z direction, i.e., for $-0.5 \leq z/d \leq 0.5$, to eliminate small perturbations. Nodes of B_z have appeared at $x/d \sim -5.8$ and -9.4 in the CS. When we refer to a “node,” we mean a pinched point of the magnetic-field structure in the CS. Such points can be defined exactly as points where B_z goes from negative to positive along the tail axis. We have estimated the wavelength of the mode as $\lambda/d \sim 4$ based on the distance between the two nodes. This wavelength is also rewritten as $kd' \sim 0.5$, where $k \equiv 2\pi/\lambda$ by adopting the thinned CS thickness d' . This wavelength is close to that reported by Bessho and Bhattacharjee (2014).

We have also calculated the growth rate of the modes that appeared in Run(0) by the following procedure.

1. Calculate the geometric average of the B_z ($z/d = 0$) during the period $0 < \Omega_i t < 4.0$. The geometric average is defined as \hat{B}_z .
2. Subtract \hat{B}_z from B_z for each time step (defined as b_z) to remove the B_z component that originally existed in the DL region.
3. Take the FFT of b_z in the x direction [we define the transformed b_z as $\tilde{b}_z(m)$], and plot the power of $\tilde{b}_z(m)$, $\left(|\tilde{b}_z(m)|^2\right)$, for each m .

Figure 4c shows the geometric average of B_z ($0 \leq \Omega_i t \leq 4$) in Run(0) resulting from procedure (1). The reason why we did not use the initial condition, $B_z(x, z = 0, t = 0)$, but have used the geometric average is that the configuration of B_z is changed by the compression of the CS during the early stages of the simulation because of the pressure difference. Figure 4d indicates the development of $\left|\tilde{b}_z(m)\right|^2$ ($m = 2, 3, 4, 5, 6$, and 8) in Run(0). $\left|\tilde{b}_z(m = 6)\right|^2$ first develops in the early stages, and this mode corresponds to the wavelength seen in Fig. 4a, $kd' \sim 0.5$. The growth rate of this mode is $\gamma/\Omega_i = 0.37$. The magnitude of this growth rate is about a half of the asymptotic

Table 1 Locations of the local B_z enhancement x_h during initial conditions

	Run(1)	Run(2)	Run(3)
x_h/d	−3.6	−5.2	−6.8

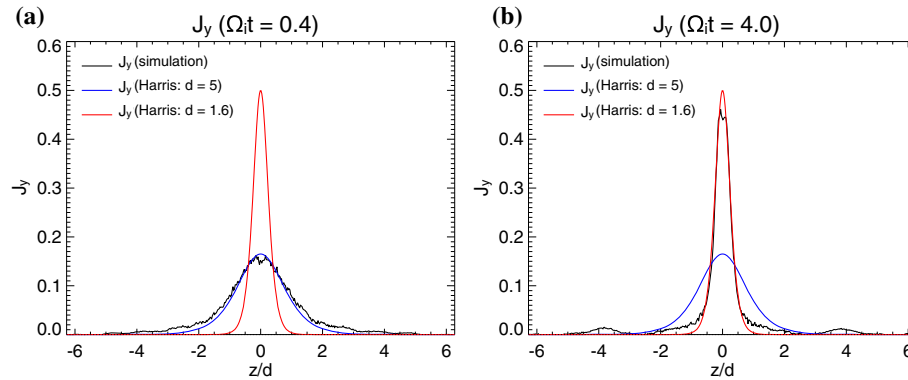


Fig. 3 Comparisons of J_y in the simulation Run(0) to the Harris solution along z . **a** J_y ($x/d = -8$) profile in the simulation (black line) follows that of the Harris solution for $d = 5$ (blue line) at the initial stage of the simulation $\Omega_i t = 0.4$. **b** J_y ($x/d = -8$) profile in the simulation (black line) follows the Harris solution for $d = 1.6$ (red line) at the time $\Omega_i t = 4.0$

electron tearing instability (Laval et al. 1966), $\gamma/\Omega_i = \sqrt{\pi} (\nu_{\text{the}}/d') (\rho_e/2d')^{3/2} [(T_i + T_e)/T_e] (1 - k^2 d'^2)/\Omega_i = 0.75$, when substituting the following parameters $\nu_{\text{the}} = 0.154c$, $\nu_{\text{th}_i} = 0.0326c$, and $d' = 1.6c/\omega_{pe}$, which are at the time of the onset $\Omega_i t = 6.8$. This growth rate compared to the theory is also consistent with the

result of “case I” in previous research by Bessho and Bhattacharjee (2014). In their simulations, the electron tearing mode showed a smaller growth rate than that of the theory by a factor of 3. We investigated the growth rates of several other tearing theories including the “ion tearing instability” ($\gamma/\Omega_i = 4.03$) by Schindler (1974),

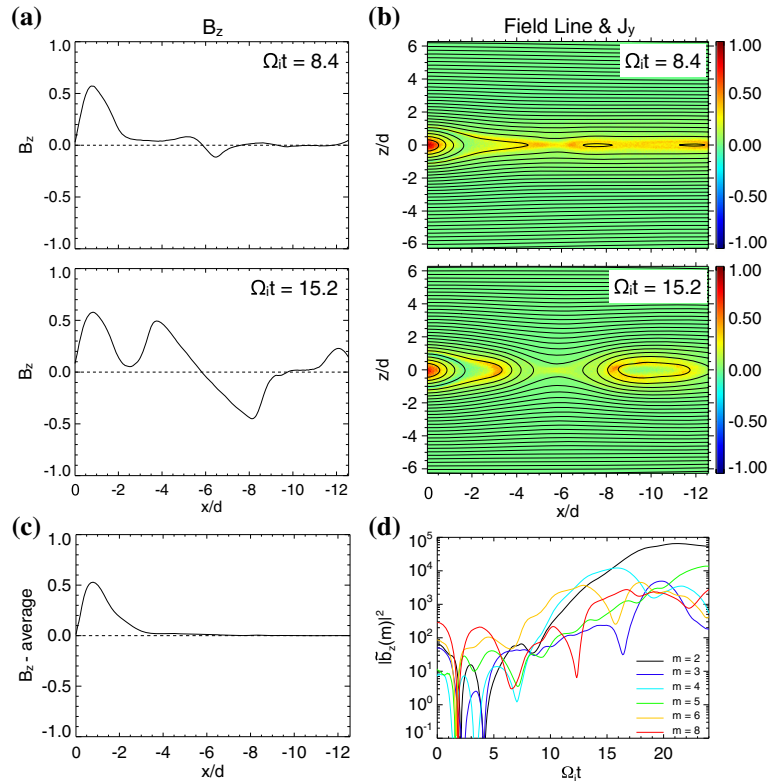


Fig. 4 Simulation results and growth rate analysis of Run(0). **a** B_z ($z/d = 0$) and **b** magnetic-field line and poloidal current J_y (color) at the times $\Omega_i t = 8.4$ and $\Omega_i t = 15.2$. **c** B_z ($z/d = 0$) averaged during the period $0 \leq \Omega_i t \leq 4.0$ in Run(0). **d** Time developments of the power of the modes resolved for B_z in Run(0)

“single particle tearing instability” ($\gamma/\Omega_i = 2.93$) by Pritchett et al. (1991), and “anisotropic tearing instability” ($\gamma/\Omega_i = 2.04$) by Quest et al. (2010), but the above theoretical growth rate is closest to our case. Therefore, this instability is likely to be electron tearing instability.

The small node of the tearing mode at $x/d \sim -9.4$ is absorbed by interactions with other nodes soon after $\Omega_i t = 8.4$. On the other hand, the node at $x/d \sim -5.8$ develops into a dominant magnetic reconnection in the simulation. The earthward flow generated by the reconnection conveys positive B_z to the DL region. This corresponds to an earthward propagating dipolarization front (Birn et al. 2011; Runov et al. 2009). The tailward flow conveying negative B_z couples with another small node of the tearing mode at $x/d \sim -13$, which appears at that location because of the mode’s periodicity, but that node cannot be seen because Fig. 4a, b does not cover that region. The dominant mode changes in correspondence with the change of the magnetic-field structure. Because a node of the tearing mode develops to a dominant magnetic reconnection and other small nodes disappear as the simulation progresses, the dominant mode number decreases from $m = 6$ to $m = 4$ in Fig. 4d. The dominant mode further decreases to $m = 2$ during the final stage of this simulation through nonlinear processes such as the coalescence of magnetic islands.

It should be noted that there are impacts of the characteristic initial conditions on the onset of the tearing instability. The normal magnetic field B_{z1} given by non-self-consistent vector potential A_{y1} decreases from 0.04 ($x/d \sim 3$) to 0 toward the tailward end. The $\mathbf{J} \times \mathbf{B}$ force resulting from incomplete force balance due to the vector potential conveys the B_z earthward. The nodes of the tearing mode, however, appear at the tailward region where the tearing growth condition $k\rho_e > 1$ is satisfied, so the above $\mathbf{J} \times \mathbf{B}$ force has less of an effect on the tearing mode in this case. By performing a three-dimensional (3D) particle-in-cell (PIC) simulation, Pritchett (2005) demonstrated that the convective electric field locally induced as a boundary condition decrements the normal field as well as the thickness of the CS locally, and once the location satisfies the growth condition $k\rho_e > 1$, tearing instability appears and develops into magnetic reconnection. On the other hand, CS thinning in our simulation does not change B_z in the CS because the magnetic flux density is not changed in the tail axis by the compression. Liu et al. (2014) conducted similar, but 2D, particle simulations to those of Pritchett (2005) and indicated that an electron tearing instability easily occurs when the anisotropy of electron $T_{e\perp}/T_{e\parallel}$ is over unity because of CS thinning. In that context, Run(0) shows a similar feature to that of Liu et al. (2014) because the electron anisotropy is $T_{e\perp}/T_{e\parallel} = 1.07$ at $\Omega_i t = 6.8$, but the wavelength in Run(0) is different from their result. Therefore, the CS thinning

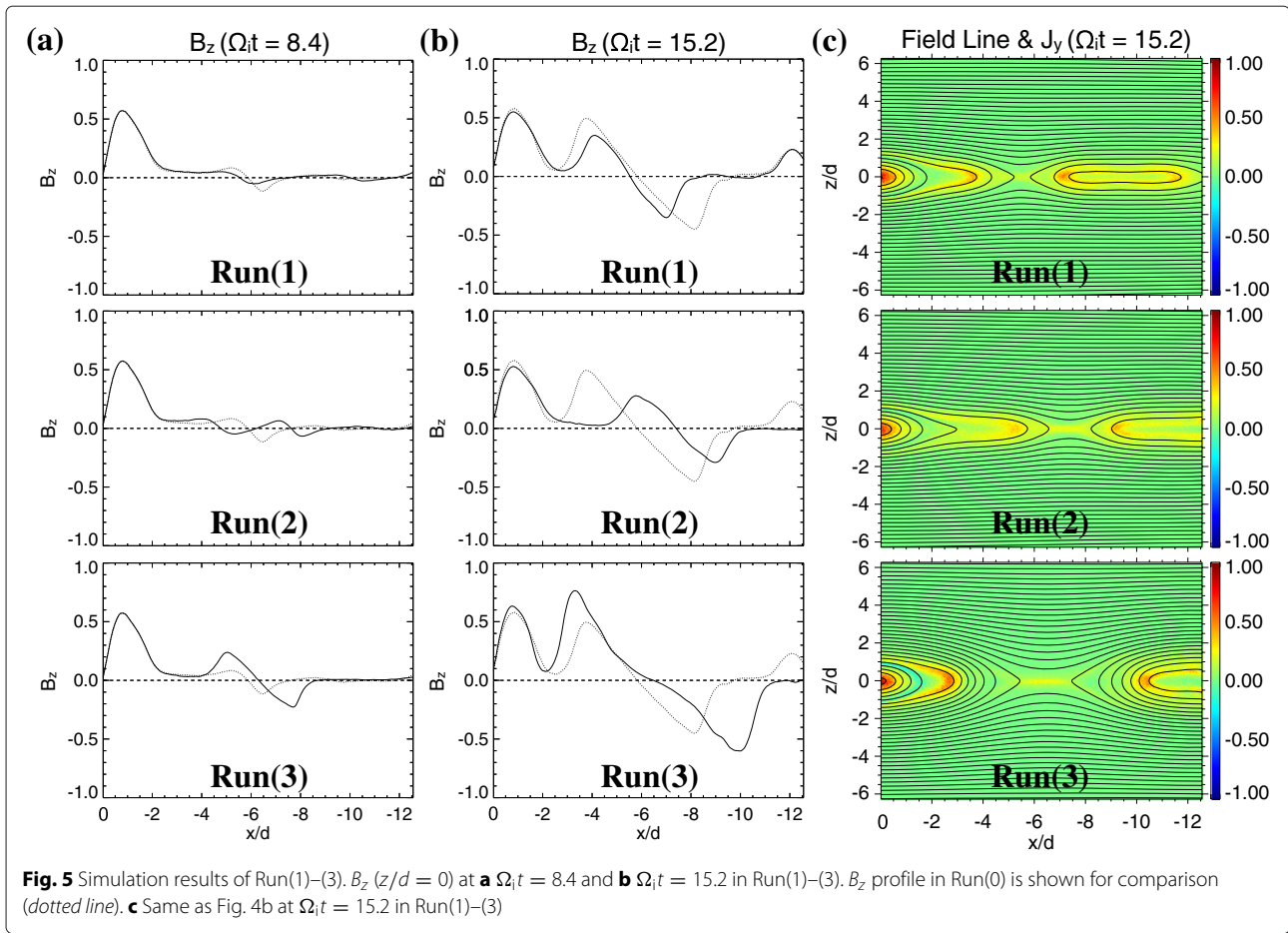
makes it easier for the instability to arise when the electron anisotropy increases, and it induces periodic nodes similar to those seen in Bessho and Bhattacharjee (2014).

Effects of the local B_z enhancement

Run(1) to Run(3) show different time developments depending on the initial locations of the local B_z enhancement seeded in the CS. Figure 5 shows B_z ($z/d = 0$) at $\Omega_i t = 8.4$ and $\Omega_i t = 15.2$, as well as the simulated magnetic-field structure and J_y at $\Omega_i t = 15.2$ of each run. The panels showing B_z ($z/d = 0$) also include the B_z component in Run(0) as a dotted line for comparison purposes.

The local enhancement in Run(1) cannot induce a node around its position because there is a strong stabilizing effect caused by the normal magnetic field around the location. The nodes of the tearing mode appear at almost the same locations ($x/d \sim -5.6, -10.1$) as those of Run(0). The node of the tearing mode at $x/d \sim -5.6$ evolves into a dominant magnetic reconnection and a dipolarization-front structure is also generated from that location [see Fig. 5b of Run(1)]. The B_z component and the magnetic-field structure are similar to those in Run(0), except that the start of the tearing onset is slightly later than that in Run(0).

In Run(2), the enhancement generates a node of B_z on its tailward side, and we found $x/d \sim -4.8$ at $\Omega_i t = 8.4$. The notion that the node (i.e., the reconnection X-point) is located on the tailward side of the local B_z enhancement is consistent with observations in which the NENL is formed on the tailward side of the local B_z enhancement (Machida et al. 2009, 2014). The reason for the appearance of the node can be considered to be the convection of the enhancement earthward by $\mathbf{J} \times \mathbf{B}$ force due to the non-self-consistency of A_{y2} . Similar relaxation processes were seen in Sitnov and Swisdak (2011) and Bessho and Bhattacharjee (2014), but they adopted a relatively large-scale B_z -hump in the CS. Even if the growth condition $k\rho_e > 1$ is not satisfied, an earthward moving B_z -hump generates the magnetic reconnection in their case. However, in our local B_z enhancement case, $k\rho_e < 1$ suppresses the instability as seen in Run(1). The local B_z enhancement is originally located in the region where the growth condition is satisfied in Run(2) and the instability has appeared. This enhancement can change the wavelength of the nodes of the tearing mode in addition to their locations. Three nodes can be found in Fig. 5a of Run(2) at $x/d \sim -4.8, -7.7$, and -10.9 ; the corresponding wavelength is $\lambda/d \sim 3$ ($kd' \sim 0.7$). We speculate that the a J_y -free region near the DCB at $x/d \sim -2$ acts as an effective boundary for the tearing mode, and the wavelength ($kd' \sim 0.7$) is defined by the distance between the effective boundary ($x/d \sim -2$) and the directly induced node ($x/d \sim -4.8$). Interestingly, the B_z profile of Run(2)



at $\Omega_i t = 15.2$ shows that the node at $x/d \sim -7.7$ (but not that at $x/d \sim -4.8$) becomes a dominant magnetic reconnection. This result reflects the fact that the growth of the instability at $x/d \sim -4.8$ is slightly suppressed by the finite normal magnetic field, while the growth of the node at $x/d \sim -7.7$ is not suppressed because $B_z \sim 0$. The growth of B_z generated by the reconnection is smaller than that seen in Run(0) at the same time, since the interaction with the node at $x/d \sim -4.8$ interferes with the growth of the instability.

Just as for Run(2), the local B_z enhancement also generates a node on its tailward side in Run(3). B_{z1} reaches almost to zero at the locus where the enhancement is seeded, and the suppression on the tearing instability is less around this region. Therefore, the enhancement quickly generates a node by the relaxation process, and the developing B_z attains a greater value than that of Run(0) at $\Omega_i t = 8.4$ and $\Omega_i t = 15.2$. In Fig. 5a, b of Run(3), the earthward flow generated by the magnetic reconnection reaches a locus close to the DL region. Enhanced plasma pressure in the DL region produced by the earthward flow decelerates the flow, and the magnetic field in the flow piles up near the DL region at $x/d \sim -3$ [see Fig. 5c of

Run(3)]. This pileup is caused by the two-dimensionality of this simulation because particles cannot escape into the y direction. This implies that the earthward flow with B_z (dipolarization front) generated by the near-Earth reconnection cannot produce the dipolarization near the DL region in 2D particle simulations.

Figures 6a, b shows the growths of the modes in Run(2) and Run(3) in the same manner as shown for Run(0). The $m = 8$ mode, which is greater than that of Run(0), becomes dominant at an early stage in Run(2). This mode corresponds to the shorter wavelength ($kd' \sim 0.7$) discussed previously. The dominant mode number decreases in a similar way to Run(0), but the dominant modes ($m = 5, 3$, and 2) are different from those seen in Run(0) because of the effects of the local B_z enhancement. In Run(3), it can be seen that the same mode numbers ($m = 6, 4$, and 2) as those in Run(0) become dominant, but these modes grow earlier. This is because the magnetic reconnection is rapidly induced by the B_z enhancement in this run. Although not shown in this paper, the time development of the modes in Run(1) is very similar to the result obtained for Run(0) since B_z in Run(0) and Run(1) exhibits similar time variations. These results confirm that the

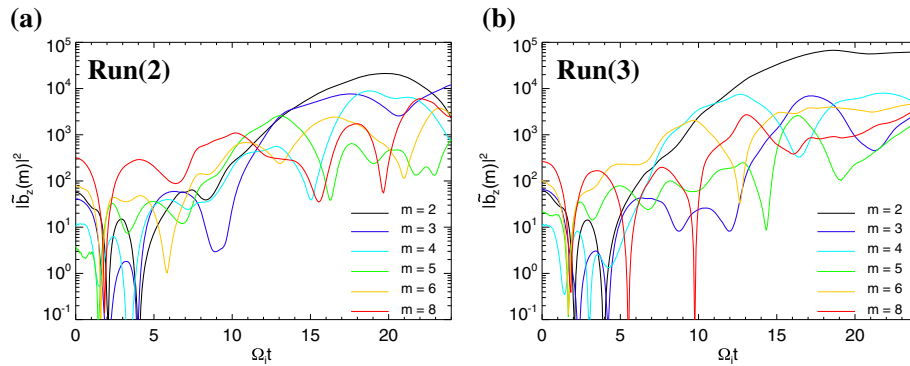


Fig. 6 Growth rate analyses for Run(2) and Run(3). **a** and **b** show time developments of the power of the modes resolved for B_z in Run(2) and Run(3), the same as Fig. 4d

local B_z enhancement can modify the mode of the tearing instability in this periodic-magnetosphere system.

Discussion and conclusions

The tearing growth condition, $k\rho_e > 1$, is rewritten as follows:

$$B_z/B_0 \leq \frac{\rho_i}{2d} \sqrt{\frac{T_e}{T_i}} \cdot \frac{m_e}{m_i}, \quad (11)$$

given that $kd' = 0.5$ and $\rho_i/d' = 1$, where ρ_i is the ion-gyro radius for B_0 (Pritchett 1994). If realistic physical quantities in the magnetotail ($\rho_i \sim d$, $T_i/T_e = 5$, and $m_i/m_e = 1836$) are substituted into the right-hand side of the following inequality, the condition for instability becomes $B_z/B_0 \leq 0.005$. In this classical view, satisfying this condition seems to be difficult, even if the CS becomes very thin before an expansion phase. Recent studies, however, have suggested that the thinning process of the CS caused by the solar wind can lead the CS to an unstable condition. Initial 2D equilibrium of an isotropic CS develops into the kinetic one-dimensional form of the anisotropic CS via the growing solar wind pressure, and the CS may become unstable for the tearing mode (Zelenyi et al. 2009). Anisotropy of electrons generated by CS thinning also facilitates the tearing mode (Liu et al. 2014; Quest et al. 2010). Therefore, we think that it is important to investigate the basic physical features of the tearing mode in the magnetosphere when discussing substorm-triggering mechanisms.

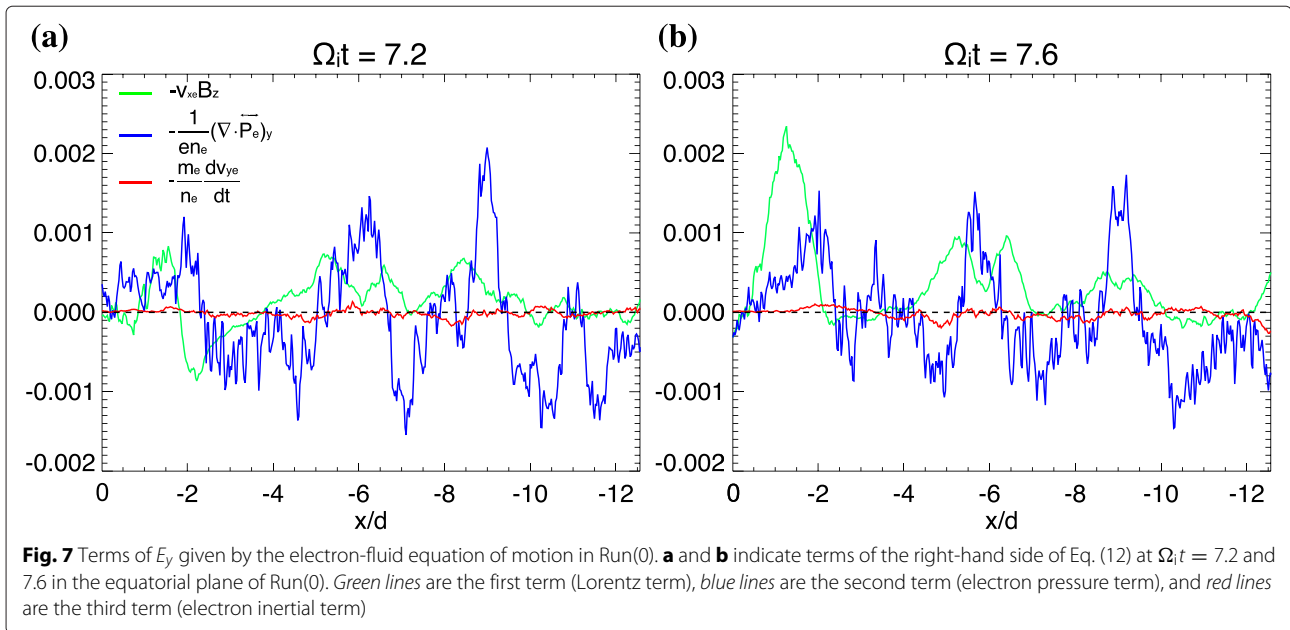
This paper focuses on the instabilities in a magnetosphere-like system spanning the regions from the DL region to the CS by employing 2.5-dimensional full-particle simulations. Based on a unique method, we have adopted a new initial magnetic-field condition for the simulations. Instabilities in the CS are rapidly induced because of the low plasma pressure. The reconnection

electric field “ E_y ” in the equatorial plane is expressed by using the electron-fluid equation of motion as follows:

$$E_y = -v_{xe}B_z - \frac{1}{en_e} \left(\frac{\partial P_{xye}}{\partial x} + \frac{\partial P_{yze}}{\partial z} \right) - \frac{m_e}{e} \frac{dv_{ye}}{dt}. \quad (12)$$

In Fig. 7, the first term (Lorentz term), second term (electron pressure term), and third term (electron inertial term) of the right-hand side at $\Omega_i t = 7.2$ and 7.6 in Run(0) are indicated by a green line, blue line, and red line, respectively. Although there are some fluctuations, the electron pressure term gives two positive peaks at $x/d \sim -6, -9$, where the nodes of the tearing mode appear. This means that the electron dynamics is crucial to the energy dissipation in the early time of the instability because the electron pressure term dominates in diffusion regions (Hesse et al. 1999; Kuznetsova et al. 2001). Therefore, we conclude that this instability is an “electron tearing instability,” even though the initial plasma sheet is not in an equilibrium state because of the low plasma pressure.

The nodes of the electron tearing mode appear in Run(0) where the growth condition is satisfied. The wavelength and growth rate of the mode show similar features to those of Bessho and Bhattacharjee (2014). In the real magnetotail, this wavelength corresponds to $\lambda \sim 3\text{Re}$, given that the thinned CS half-thickness is $d' \sim 1500$ km during substorms (Asano et al. 2004). This wavelength is shorter than the average distance between the DCB and NENL by a factor of 3–4, but it is consistent with the observation of the magnetic flux rope produced by a few Re spatial scales of multiple X-lines (Eastwood et al. 2005). If it is assumed that the J_y -free region near the DCB acts as an effective boundary for the tearing mode, such multiple X-lines may appear at the specific locations with each wavelength corresponding to the condition of the magnetosphere.



Three additional simulations with the local B_z enhancement included in the CS region, as observed by Machida et al. (2009, 2014), were performed. We found that in Run(1), where the enhancement is located near the DCB, nodes of the tearing instability appeared at similar loci as in Run(0) because the normal magnetic-field component of B_{z1} suppresses the instability at that site. However, the local enhancement located tailward from the DCB induces a node of B_z on its tailward edge in Run(2) and Run(3) because of the relaxation process caused by the local enhancement. This result is similar to the findings of previous research (Bessho and Bhattacharjee 2014; Sitnov and Swisdak 2011). This also can explain the observations showing magnetic reconnection on the tailward side of the B_z enhancement at the substorm onset (Machida et al. 2009, 2014). An interesting result is obtained in regard to the location of the main node of the tearing instability, which develops into the X-point of a dominant magnetic reconnection. The node, which is preferentially induced tailward of the local B_z enhancement, develops into a dominant reconnection X-point in Run(3). In Run(2), however, the induced node does not develop into a dominant reconnection, but the node located one wavelength down the tailward direction becomes a dominant X-point. This is because a greater normal magnetic field B_{z1} at the earthward node than that at the tailward region impairs the growth of the instability more effectively. This result implies that, even if such a local B_z enhancement induces a node of the tearing mode during the substorm period, the nodes at one (or several) wavelength(s) tailward of the node may develop into a magnetic reconnection depending on the locus of the enhancement with respect to the background normal B_z component.

We found that the enhancement changes the wavelength and mode number particularly in Run(2) by coupling between the relaxation process and the tearing n. Rapid appearance of the instability by the CS thinning from the initial pressure difference caused such coupling. Even if such a local enhancement exists, the change of the wavelength of the tearing mode may not occur in the real magnetotail because it is possibly caused by the boundary conditions in the x direction; hence, this result requires a reassessment of the boundary conditions. That is an aspect of our future work. We have also shown that a dominant mode of the tearing instability switches because of the influence of nonlinear effects, such as the coalescence of magnetic islands, as the simulations progress.

In this study, we had to deal with several free parameters that define the form of the magnetospheric system. We note that p and ϵ_2 are particularly important. As p , which defines the roundness of the DL region, decreases, the shape of the region becomes closer to that of the Harris sheet and the J_y -free region is not formed. A smaller value of ϵ_2 than what was adopted may not preferentially induce nodes of the tearing instability. Nevertheless, the ratios determined by these two parameters, $B_{z0} : B_0 = 1 : 2$ (B_{z0} ; the maximum of B_z in the DL region, B_0 ; B_x in the lobe region) and $B_{z0} : B_{z2} = 10 : 1$ (B_{z2} ; the maximum of B_{z2}), do not deviate significantly from the observations (Machida et al. 2009, 2014).

The local B_z enhancement has been included artificially in this study, but why and how such an enhancement exists at $X \sim -17$ Re prior to substorm onset is still an open question. One possibility is that the enhancement is produced by an interaction between the thinning process of the CS and the earthward flows with a

small B_z component that propagate from a distant neutral line. More extensive observations or sophisticated simulations are necessary to further investigate this problem. The physical mechanism related to dipolarization has not occurred in our simulations, but CD is also statistically expected to occur simultaneously with magnetic reconnection around the DCB (Machida et al. 2009, 2014; Miyashita et al. 2009). The DL region's shape and size remain almost constant in the simulations, despite the development of a tearing instability in the CS. This implies that because the DL region acts as an effective boundary for the tearing mode, the tearing mode cannot directly affect the physical processes in the DL region. Therefore, CD is considered to be the consequence of other types of instabilities. One of the limitations is that in a 2D system, any possible couplings between a tearing mode and other instabilities cannot be modeled properly. In the future, we plan to use full 3D simulations to investigate whether such couplings occur or not.

Competing interests

The authors declare that they have no competing interests.

Authors' contribution

HU carried out all simulations, analyzed the simulation data, and wrote the manuscript. SM made the basic simulation code and helped in interpretation of the data. Both authors read and approved the final manuscript.

Acknowledgements

We used CX250 at Nagoya University for simulations in this research. This research has been partially supported by a Grant-in-Aid from the Japan Society for the Promotion of Science (JSPS) Fellows (26–655) program. H. Uchino was supported by a research fellowship from the JSPS Young Scientists program.

Author details

¹Department of Geophysics, Kyoto University, Kyoto, Japan. ²Solar Terrestrial Environment Laboratory, Nagoya University, Aichi, Japan.

Received: 29 April 2015 Accepted: 23 September 2015

Published: 8 October 2015

References

- Akasofu S-I (1964) The development of the auroral substorm. *Planet Space Sci* 12:273–82. doi:10.1016/0032-0633(64)90151-5
- Asano Y, Mukai T, Hoshino M, Saito Y, Hayakawa H, Nagai T (2004) Statistical study of thin current sheet evolution around substorm onset. *J Geophys Res* 109:A05213. doi:10.1029/2004JA010413
- Baker DN, Pulkkinen TI, Angelopoulos V, Baumjohann W, McPherron RL (1996) Neutral line model of substorms: past results and present view. *J Geophys Res* 101:12975–3010. doi:10.1029/95JA03753
- Bessho N, Bhattacharjee A (2014) Instability of the current sheet in the Earth's magnetotail with normal magnetic field. *Phys Plasmas* 21:102905. doi:10.1063/1.4.899043
- Birdsall CK, Langdon AB (1985) *Plasma physics via computer simulation*. McGraw-Hill, New York
- Birn J, Drake JF, Shay MA, Rogers BN, Denton RE, Hesse M, Kuznetsova M, Ma ZW, Bhattacharjee A, Otto A, Pritchett PL (2001) Geospace Environmental Modeling (GEM) Magnetic Reconnection Challenge. *J Geophys Res* 106:3715–9. doi:10.1029/1999JA900449
- Birn J, Nakamura R, Panov EV, Hesse M (2011) Bursty bulk flows and dipolarization in MHD simulations of magnetotail reconnection. *J Geophys Res* 116:A01210. doi:10.1029/2010JA016083
- Chao JK, Kan JR, Lui ATY, Akasofu SI (1977) A model for thinning of plasma sheet. *Planet Space Sci* 25:703–10. doi:10.1016/0032-0633(77)90122-2
- Dreher J, Arendt U, Schindler K (1996) Particle simulations of collisionless reconnection in magnetotail configuration including electron dynamics. *J Geophys Res* 101:27375–81. doi:10.1029/96JA02040
- Eastwood JP, Sibeck DG, Slavin JA, Goldstein ML, Lavraud B, Sitnov M, Imber S, Balogh A, Lucek EA, Dandouras I (2005) Observations of multiple X-line structure in the Earth's magnetotail current sheet: a cluster case study. *Geophys Res Lett* 32:L11105. doi:10.1029/2005GL022509
- Hesse M, Schindler K, Birn J, Kuznetsova M (1999) The diffusion region in collisionless magnetic reconnection. *Phys Plasmas* 6:1781–95. doi:10.1063/1.873436
- Hones EW Jr (1979) Transient phenomena in the magnetotail and their relation to substorms. *Space Sci Rev* 23:393–410. doi:10.1007/BF00172247
- Kuznetsova M, Hesse M, Winske D (2001) Collisionless reconnection supported by nongyrotropic pressure effects in hybrid and particle simulations. *J Geophys Res* 106:3799–810. doi:10.1029/1999JA001003
- Laval G, Pellat R, Vuirremin M (1966) Electromagnetic instabilities in a collisionless plasma. In: *Plasma Physics and Controlled Nuclear Fusion Research. Vol. II. Proceedings of Conference on Plasma Physics and Controlled Nuclear Fusion Research*. International Atomic Energy Agency, Vienna. pp 259–277
- Lui ATY (1991) A synthesis of magnetospheric substorm models. *J Geophys Res* 96:1849–56. doi:10.1029/90JA02430
- Lui, ATY (1996) Current disruption in the Earth's magnetosphere: observations and models. *J Geophys Res* 101:13067–88. doi:10.1029/96JA00079
- Liu Y-H, Birn J, Daughton W, Heese M, Schindler K (2014) Onset of reconnection in the near magnetotail: PIC simulations. *J Geophys Res Space Phys* 119:9773–89. doi:10.1002/2014JA020492
- Machida S, Miyashita Y, Ieda A, Nosé M, Nagata D, Liou K, Obara T, Nishida A, Saito Y, Mukai T (2009) Statistical visualization of the Earth's magnetotail based on Geotail data and the implied substorm model. *Ann Geophys* 27:1035–46. doi:10.5194/angeo-27-1035-2009
- Machida S, Miyashita Y, Ieda A, Nosé M, Angelopoulos V, McFadden JP (2014) Statistical visualization of the Earth's magnetotail and the implied mechanism of substorm triggering based on superposed-epoch analysis of THEMIS data. *Ann Geophys* 32:99–111. doi:10.5194/angeo-32-99-2014
- Miyashita Y, Machida S, Kamide Y, Nagata D, Liou K, Fujimoto M, Ieda A, Saito MH, Russell CT, Christon SP, Nosé M, Frey HU, Shinohara I, Mukai T, Saito Y, Hayakawa H (2009) A state-of-the-art picture of substorm-associated evolution of the near-Earth magnetotail obtained from superposed epoch analysis. *J Geophys Res* 114:A01211. doi:10.1029/2008JA013225
- Pellat R, Coroniti FV, Pritchett PL (1991) Does ion tearing exist? *Geophys Res Lett* 18:143–6. doi:10.1029/91GL00123
- Pritchett PL, Coroniti FV, Pellat R, Karimabadi H (1991) Collisionless reconnection in two-dimensional magnetotail equilibria. *J Geophys Res* 96:11523–38. doi:10.1029/91JA01094
- Pritchett PL (1994) Effect of electron dynamics on collisionless reconnection in two-dimensional magnetotail equilibria. *J Geophys Res* 99:5935–41. doi:10.1029/93JA03297
- Pritchett, PL (2005) Externally driven magnetic reconnection in the presence of a normal magnetic field. *J Geophys Res* 110:A05209. doi:10.1029/2004JA010948
- Quest KB, Karimabadi H, Daughton W (2010) Linear theory of anisotropy driven modes in a Harris neutral sheet. *Phys Plasmas* 17:022107. doi:10.1063/1.3309731
- Runov A, Angelopoulos V, Sitnov MI, Sergeev VA, Bonnell J, McFadden JP, Larson D, Glassmeier K-H, Auster U (2009) THEMIS observations of an earthward-propagating dipolarization front. *Geophys Res Lett* 36:L14106. doi:10.1029/2009GL038980
- Schindler K (1974) A theory of the substorm mechanism. *J Geophys Res* 79:2803–10. doi:10.1029/JA079i019p02803
- Schindler K (2007) *Physics of space plasma activity*. Cambridge Univ. Press, New York
- Shiokawa K, Baumjohann W, Haerendel G, Paschmann G, Fennell JF, Friis-Christensen E, Lühr H, Reeves GD, Russell CT, Sutcliffe PR, Takahashi K (1998) High-speed ion flow, substorm current wedge, and multiple Pi 2 pulsations. *J Geophys Res* 103:4491–507. doi:10.1029/97JA01680
- Sitnov MI, Swisdak M (2011) Onset of collisionless magnetic reconnection in two-dimensional current sheets and formation of dipolarization fronts. *J Geophys Res* 116:A12216. doi:10.1029/2011JA016920
- Toichi T (1972) Two-dimensional equilibrium solution of the plasma sheet and its application to the problem of the tail magnetosphere. *Cosmic Electrodynamic* 3:81–96

- Voigt GH (1986) Magnetospheric equilibrium configurations and slow adiabatic convection, solar wind-magnetosphere coupling. In: Kamide Y, Slavin J (eds). *Solar Wind and Magnetosphere Couplings*. Tokyo, Terra Sci. pp 233–273
- Zelenyi LM, Kropotkin AP, Domrin VI, Artemyev AV, Malova HV, Popov VY (2009) Tearing mode in thin current sheets of the Earth's magnetosphere: a scenario of transition to unstable state. *Cosmic Res* 47:352–60. doi:10.1134/S0010952509050025
- Zwingmann W, Wallace J, Schindler K, Birn J (1990) Particle simulation of magnetic reconnection in the magnetotail configuration. *J Geophys Res* 95:20877–88. doi:10.1029/JA095iA12p20877

Submit your manuscript to a SpringerOpen[®] journal and benefit from:

- Convenient online submission
- Rigorous peer review
- Immediate publication on acceptance
- Open access: articles freely available online
- High visibility within the field
- Retaining the copyright to your article

Submit your next manuscript at ► [springeropen.com](https://www.springeropen.com)
